Dyes and Pigments 187 (2021) 109076

Contents lists available at ScienceDirect

Dyes and Pigments

journal homepage: http://www.elsevier.com/locate/dyepig

Fabrication of strongly near-infrared absorbing vesicles by stabilizing chromogenic radicals in biomimetic membranes

Yang Chen [a], Juanmei Zeng [a], Wenchao Huang [b], Yuanmei Hu [a], Shunhua Li [a,*], Yunbao Jiang [a]

[a] Department of Chemistry and the MOE Key Laboratory of Spectrochemical Analysis & Instrumentation, College of Chemistry and Chemical Engineering, Xiamen University, Xiamen, 361005, China

[b] State Key Laboratory of Molecular Vaccinology and Molecular Diagnostics, Centre for Molecular Imaging and Translational Medicine, School of Public Health, Xiamen University, Xiamen, 361102, PR China

ARTICLE INFO

Keywords:
Near-infrared dyes
Vesicles
Radicals
Self-assembly
Photoacoustic imaging

ABSTRACT

An efficient approach for fabrication of novel near-infrared (NIR) absorbing materials has been developed based on stabilization of chromogenic radicals in lipid membranes. Compared with the closed-shell molecules, radicals or radical ions of organic chromophores usually display remarkably red-shifted absorption. However, stabilization and functionalization of these radicals is still a challenging task. Herein, biomimetic membranes were employed as a platform for stabilization and convenient functionalization of chromogenic radicals. NIR optical vesicles can be facilely formed by co-assembly of radical-dominated supramolecular chromophores with surfactants in aqueous solution. The as-formed dye-interbedded vesicles with biomimetic membrane surfaces displays strong NIR absorption and electron spin resonance signals, sensitive photoacoustic response upon NIR excitation, and minimal nonspecific interaction with biological macro-molecules. Furthermore, doping of the chromogenic interlayers to optimize the optical properties and modification of the membrane surfaces for functionalization towards bioanalytical applications can be carried out under ambient conditions.

1. Introduction

Near-infrared (NIR) light is highly applicable to optical exploring of biological systems because of its deeper tissue penetration, minimal photo-damage, and reduced background interference [1–5]. Design of high-performance NIR dyes [6–12] or nanoprobes [13–18] has been attracting intense interest in bioanalytical and biomedical researches. In general, the NIR response of organic dyes arises from a large conjugation system. Therefore, difficulty in both synthesis and modification of NIR dyes remains a challenge in their advanced applications [19–24]. It is known that the band gap between the lowest singly unoccupied molecular orbital (SUMO) and the singly occupied molecular orbital (SOMO) of an organic radical is much narrower than that between the lowest unoccupied molecular orbital (LUMO) and the highest occupied molecular orbital (HOMO) of its closed-shell molecule [25,26]. This has boosted a new class of NIR dyes based on radicals or radical ions of common organic chromophores in the ultraviolet–visible region, as exemplified by the radical anions of aromatic imides with high photothermal conversion efficiency upon NIR irradiation [27–34]. Taking advantage of the ease in generating organic radicals from their closed-shell molecules by chemical or biological methods, novel stimuli-responsive NIR optical materials can be developed [32,35,36]. However, stabilization and functionalization of radical-based NIR dyes is still challenging in their biological applications. Herein, biomimetic membranes were employed as a platform for stabilization and convenient functionalization of organic radicals to give the first example of radical-interbedded NIR absorbing vesicles.

The radical anion of tetrafluorotetracyanoquinodimethane ($TCNQF_4$) was investigated as the NIR absorber in this study. The NIR absorption of the radical anion of tetracyano-*p*-quinodimethane (TCNQ) has long been known [37]. Most of the analogues of $TCNQ^{\bullet -}$ were stabilized in the form of solid salts and research attention has been focused on their conductivity and magnetism [37–39]. Bioanalytical and biomedical applications of these radical anions as NIR dyes remain unexplored because of their low stability in aqueous solution and difficulty in functionalization. We proposed that degradation of these chromogenic radicals would be greatly prevented in lipid membranes and further functionalization could be easily realized through modifications of the membrane surfaces. For this purpose, the radical-based NIR absorber was produced and handled in the form of supramolecular dyad,

* Corresponding author.
E-mail address: lishua@xmu.edu.cn (S. Li).

https://doi.org/10.1016/j.dyepig.2020.109076
Received 15 June 2020; Received in revised form 8 October 2020; Accepted 6 December 2020
Available online 13 December 2020
0143-7208/

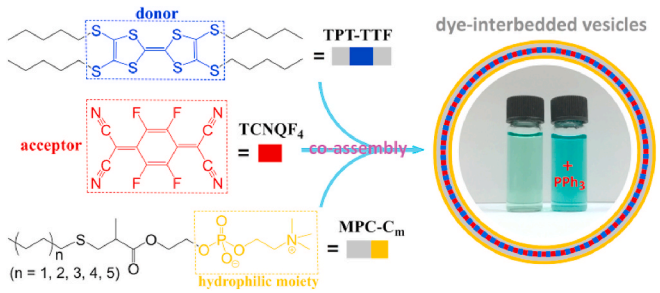

Scheme 1. Illustration of the fabrication of $TCNQF_4^{\bullet-}$-interbedded vesicles in aqueous solution.

following the discovery in 1973 that $TCNQ^{\bullet-}$ could be *in situ* generated in the conducting donor-acceptor (D-A) complex between tetrathiofulvalene (TTF) and TCNQ [40]. Tetrakis(pentyl-thio)tetrathiafulvalene (TPT-TTF) and $TCNQF_4$ were chosen as the electron donor and the electron acceptor [41], respectively, to enhance the charge transfer that leads to radical ions (Scheme 1). On the other hand, the structural feature that TPT-TTF contains symmetrical four hydrophobic chains would facilitate co-assembling of the π-aggregated NIR chromogenic ensembles with amphiphiles in aqueous solutions driven by hydrophobic interaction. To improve biocompatibility of the resulting co-assemblies, the model amphiphiles were designed to bear phosphorylcholine, known as the head group of phospholipid, as the hydrophilic group.

2. Experimental

2.1. General remarks

All syntheses were performed under a nitrogen atmosphere using standard Schlenk techniques, unless otherwise stated. Acetonitrile were distilled from calcium hydride under N_2 prior to use. Other reagents were used as received from commercial sources without further purification.

Absorption spectra were recorded on a Hitachi U-3900 UV–Vis spectrophotometer or a Vavian Cary 5000 UV–Vis–NIR spectrophotometer. Electrospray ionisation (ESI) mass spectra were recorded on a Bruker ESQUIRE-3000$^+$ mass spectrometer. High-resolution mass spectra (HR-MS) were recorded on a Bruker Apex ultra 7.0T FT-ICR mass spectrometer. The nuclear magnetic resonance (NMR) experiments were performed on a Bruker Avance II 400 MHz spectrometer. ^{1}H and ^{13}C NMR chemical shifts (δ) are relative to tetramethylsilane. The absolute values of the coupling constants are given in Hertz (Hz). Multiplicities are abbreviated as singlet (s), doublet (d), triplet (t), multiplet (m) and broad (br). Dynamic light scattering (DLS) data were collected from a Malvern Zetasizer Nano-zsMPT-2 particle size and zeta potential analyzer. Infrared spectra were recorded on a Nicolet AVATAR FT-IR360 spectrophotometer. Morphologic evolutions of the self-assemblies were studied by a Tecnai G2 Spirit BioTwin transmission electron microscope (TEM). Photoacoustic responses were examined on a Vevo®3100 preclinical imaging system with a pulsed 850 nm laser.

2.2. Synthesis and characterization of *MPC-C_m*

Thiol (0.4 mmol) with a predesigned alkyl group was added to a solution of 2-(methacryloyloxy)ethyl 2-(trimethylammonio)ethyl phosphate (MPC, 0.40 mmol) in anhydrous ethanol (15 mL). The mixture was stirred at room temperature in nitrogen atmosphere for 20 h in the presence of 1,3-propanediamine (catalytic amount). The solvent was then removed under vacuum. The resulting viscous mixture was washed with n-hexane, acetone and anhydrous ethanol successively in ultrasound, and dried under vacuum to give a translucent solid with a high yield (> 93%). All of the MPC-C_m compounds in KBr matrix share a same absorption profile in FT-IR spectra: ν_{max}/cm^{-1} = 1734 (C═O), 1247 (P═O), 1084 (P–O), 965 (-NMe_3^+).

The selected spectroscopic data of **MPC-C_4** are as follows. ^{1}H NMR (CD_3OD, 400 MHz, ppm): δ = 0.92 (t, *J* 7.2, $CH_3CH_2CH_2$-, 3H), 1.23 (d, *J* 6.8, –CH(CH_3)CO-, 3H), 1.36–1.42 (m, *J* 7.2, $CH_3CH_2CH_2$-, 2H), 1.53–1.57 (m, *J* 7.2, -$CH_2CH_2CH_2$S-, 2H), 2.51–2.81 (m, *J* 6.8, 7.2, -$CH_2CH_2SCH_2CH(CH_3)$-, 5H), 3.23 (s, –N(CH_3)$_3$, 9H), 3.63–3.65 (m, *J* 5.2, -CH_2N, 2H), 4.05–4.09 (m, *J* 5.2, POCH_2-, 2H), 4.26–4.29 (m, *J* 5.2, OCH_2CH_2OP, 4H). ^{13}C NMR (CD_3OD, 125 MHz, ppm): δ = 175.40, 66.08, 63.85, 63.30, 59.04, 53.33, 40.21, 34.90, 31.69, 31.48, 21.48, 15.78, 12.60. ESI-MS: *m/z* calc. 386.1 $[M + H]^+$; found 386.0 and 408.0 $[M + Na]^+$; HR-MS (ESI): *m/z* calc. 408.1580 $[M + Na]^+$; found 408.1584 with expected isotopic distribution.

The selected spectroscopic data of **MPC-C_6** are as follows. ^{1}H NMR (CD_3OD, 400 MHz, ppm): δ = 0.91 (t, *J* 7.0, $CH_3CH_2CH_2$-, 3H), 1.23 (d, *J* 7.2, –CH(CH_3)CO, 3H), 1.32–1.41 (m, *J* 7.2, $CH_3CH_2CH_2CH_2CH_2$-, 6H), 1.54–1.58 (m, *J* 7.2, -$CH_2CH_2CH_2$S-, 2H), 2.50–2.81 (m, *J* 6.8, 7.2, -$CH_2CH_2SCH_2CH(CH_3)$-, 5H), 3.23 (s, –N(CH_3)$_3$, 9H), 3.63–3.66 (m, *J* 5.2, -CH_2N, 2H), 4.05–4.09 (m, *J* 5.2, POCH_2-, 2H), 4.26–4.29 (m, *J* 5.2, OCH_2CH_2OP, 4H). ^{13}C NMR (CD_3OD, 125 MHz, ppm): δ = 175.40, 66.08, 64.06, 63.07, 59.32, 54.26, 40.18, 35.38, 32.79, 31.41, 29.64, 28.54, 22.54, 16.94, 14.03. ESI-MS: *m/z* calc. 414.2 $[M + H]^+$; found 414.0 and 436.0 $[M + Na]^+$. HR-MS (ESI): *m/z* calc. 436.1893 $[M + Na]^+$; found 436.1889 with expected isotopic distribution.

The selected spectroscopic data of **MPC-C_7** are as follows. ^{1}H NMR (CD_3OD, 400 MHz, ppm): δ = 0.90 (t, *J* 6.8, $CH_3CH_2CH_2$-, 3H), 1.23 (d, *J* 7.2, –CH(CH_3)CO-, 3H), 1.30–1.39 (m, *J* 7.2, $CH_3CH_2CH_2CH_2CH_2CH_2$-, 8H), 1.54–1.58 (m, *J* 7.2, -$CH_2CH_2CH_2$S-, 2H), 2.50–2.81 (m, *J* 6.8, 7.2, -$CH_2CH_2SCH_2CH(CH_3)$-, 5H), 3.23 (s, –N(CH_3)$_3$, 9H), 3.63–3.66 (m, *J* 5.2, -CH_2N, 2H), 4.05–4.09 (m, *J* 5.2, POCH_2-, 2H), 4.26–4.30 (m, *J* 5.2, OCH_2CH_2OP, 4H). ^{13}C NMR (CD_3OD, 125 MHz, ppm): δ = 175.40, 66.08, 63.86, 63.80, 63.26, 59.05, 53.34, 40.21, 34.90, 32.02, 31.54, 29.36, 28.62, 28.41, 22.27, 15.81, 13.04. ESI-MS: *m/z* calc. 428.2 $[M + H]^+$; found 428.0 and 450.2 $[M + Na]^+$. HR-MS (ESI): *m/z* calc. 450.2049 $[M + Na]^+$; found 450.2055 with expected isotopic distribution.

The selected spectroscopic data of **MPC-C_8** are as follows. ^{1}H NMR (CD_3OD, 400 MHz, ppm): δ = 0.90 (t, *J* 6.8, $CH_3CH_2CH_2$-, 3H), 1.23 (d, *J* 7.2, –CH(CH_3)CO-, 3H), 1.30–139 (m, *J* 7.2, $CH_3CH_2CH_2CH_2CH_2CH_2$CH$_2$-, 10H), 1.52–1.60 (m, *J* 7.2, -$CH_2CH_2CH_2$S-, 2H), 2.50–2.81 (m, *J* 6.8, 7.2, -$CH_2CH_2SCH_2CH(CH_3)$-, 5H), 3.22 (s, –N(CH_3)$_3$, 9H), 3.63–3.66 (m, *J* 5.2, -CH_2N, 2H), 4.05–4.09 (m, *J* 5.2, POCH_2-, 2H), 4.28–4.30 (m, *J* 5.6, OCH_2CH_2OP, 4H). ^{13}C NMR (CD_3OD, 125 MHz, ppm): δ = 175.41, 66.08, 63.86, 63.80, 63.31, 63.26, 59.06, 59.02, 53.38, 53.35, 53.32, 40.21, 34.90, 32.03, 31.59, 29.35, 28.96, 28.90, 28.45, 22.31, 17.05, 15.82, 13.06. ESI-MS: *m/z* calc. 442.2 $[M + H]^+$; found 442.1 and 464.1 $[M + Na]^+$. HR-MS (ESI): *m/z* calc. 464.2206 $[M + Na]^+$; found 464.2206 with expected isotopic distribution.

The selected spectroscopic data of **MPC-C_{10}** are as follows. ^{1}H NMR (CD_3OD, 400 MHz, ppm): δ = 0.90 (t, *J* 7.0, $CH_3CH_2CH_2$-, 3H), 1.23 (d, *J* 7.2, –CH(CH_3)CO-, 3H), 1.29–1.38 (m, *J* 7.2, $CH_3CH_2CH_2CH_2CH_2CH_2CH_2CH_2CH_2$-, 14H), 1.54–1.58 (m, *J* 7.2, -$CH_2CH_2CH_2$S-, 2H), 2.50–2.81 (m, *J* 6.8, 7.2, -$CH_2CH_2SCH_2CH(CH_3)$-, 5H), 3.23 (s, –N(CH_3)$_3$, 9H), 3.63–3.66 (m, *J* 5.2, -CH_2N, 2H), 4.05–4.09 (m, *J* 5.2, POCH_2-, 2H), 4.26–4.30 (m, *J* 5.6, OCH_2CH_2OP, 4H). ^{13}C NMR (CD_3OD, 125 MHz, ppm): δ = 175.40, 66.08, 63.86, 63.80, 63.31, 63.26, 59.05, 59.01, 53.37, 53.34, 53.31, 34.90, 32.03, 31.67, 29.35, 29.29, 29.05, 28.94, 28.45, 22.34, 15.82, 13.07. ESI-MS: *m/z* calc. 470.2 $[M + H]^+$; found 470.1 and 492.2 $[M + Na]^+$. HR-MS (ESI): *m/z* calc. 492.2519 $[M + Na]^+$; found 492.2516 with expected isotopic distribution.

The selected spectroscopic data of **MPC-C_{12}** are as follows. ^{1}H NMR (CD_3OD, 400 MHz, ppm): δ = 0.90 (t, *J* 6.8, $CH_3CH_2CH_2$-, 3H), 1.23 (d, *J* 7.2, –CH(CH_3)CO-, 3H), 1.29–1.38 (m, *J* 7.2,

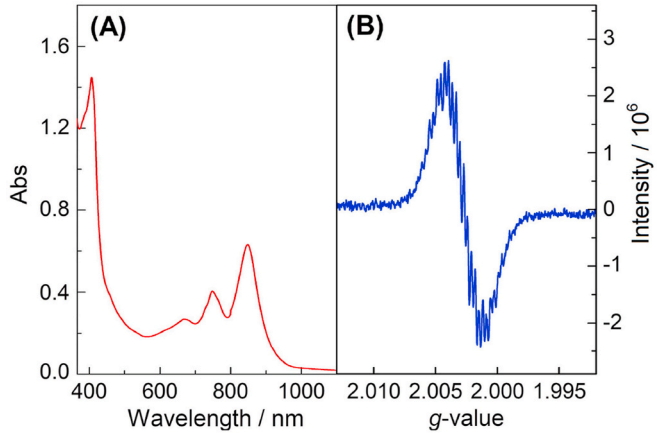

Fig. 1. Absorption (A) and ESR (B) spectra of the co-assemblies of TPT-TTF (50 μM), $TCNQF_4$ and MPC-C_8 at a molar ratio of 1 : 1 : 4 in aqueous solution at pH 7.4 (buffered by 10 mM 3,3-dimethylglutaric acid-NaOH).

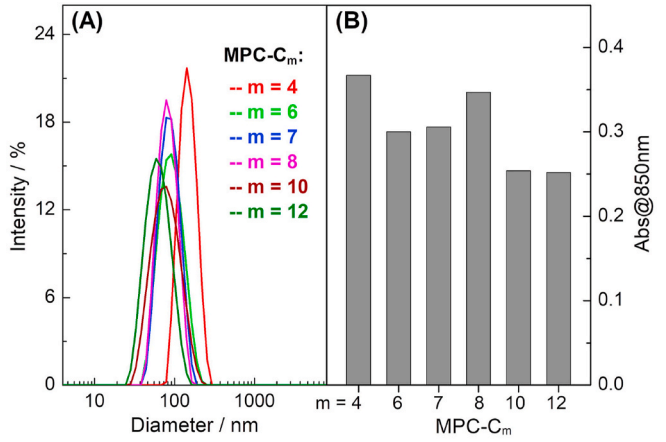

Fig. 2. Size distributions (A) and absorption spectra (B) of the co-assemblies of TPT-TTF (32 μM), $TCNQF_4$ (24 μM) and MPC-C_m (128 μM) in aqueous solution at pH 7.4 (buffered by 10 mM 3,3-dimethylglutaric acid-NaOH).

$CH_3CH_2CH_2CH_2CH_2CH_2CH_2CH_2CH_2CH_2CH_2$-, 18H), 1.52–1.58 (m, *J* 7.2 -$CH_2CH_2CH_2S$-, 2H), 2.50–2.81 (m, *J* 6.8, 7.2, -$CH_2CH_2SCH_2CH(CH_3)$-, 5H), 3.23 (s, –$N(CH_3)_3$, 9H), 3.63–3.65 (m, *J* 5.2, -CH_2N, 2H), 4.05–4.09 (m, *J* 5.2, $POCH_2$-, 2H), 4.26–4.30 (m, *J* 5.6, OCH_2CH_2OP, 4H). ^{13}C NMR (CD_3OD, 125 MHz, ppm): $\delta = 175.51, 66.09, 63.85, 63.79, 63.31, 63.26, 59.05, 59.01, 53.36, 53.33, 53.31, 40.21, 34.91, 32.03, 31.68, 29.37, 29.35, 29.28, 29.07, 28.94, 28.45, 22.34, 15.81$. HR-MS (ESI): *m/z* calc. 520.2832 $[M + Na]^+$; found 520.2834 with expected isotopic distribution.

3. Results and discussion

3.1. Fabrication of the NIR absorbing vesicles

NIR absorbing nanovesicles were facilely fabricated via self-assembly. The chromogenic D-A dyads were formed by self-assembly of TPT-TTF and $TCNQF_4$ in acetonitrile. This solution was next mixed with aqueous solution of different types of amphiphiles to yield nanostructured co-assemblies after evaporation of the organic solvent. Fig. 1A shows the absorption spectrum of a solution of the co-assemblies of 1 : 1 D-A ensemble with MPC-C_8 with peaks at 407, 670, 749 and 850 nm, respectively, indicating the formation of $TCNQF_4^{\bullet-}$ [39,42]. Accompanying the characteristic NIR absorption, a strong electron spin resonance (ESR) signal was observed at $g = 2.0029$ with hyperfine

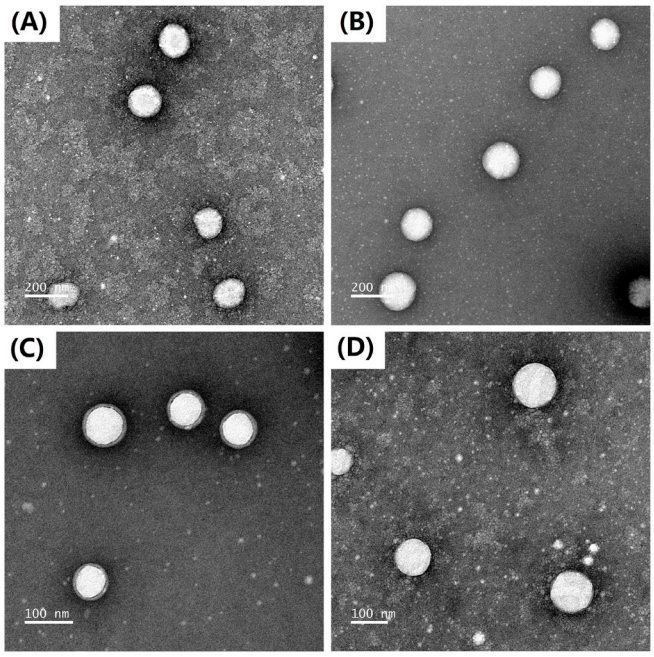

Fig. 3. TEM images of the vesicles resulting from the co-assembly of TPT-TTF (40 μM), $TCNQF_4$ (30 μM) with different surfactants or dopants in aqueous solution at pH 7.4 (buffered by 10 mM 3,3-dimethylglutaric acid-NaOH). Surfactants and dopants: (A) 160 μM MPC-C_8, no dopant; (B) 160 μM MPC-C_8, 14 μM PPh_3; (C) 160 μM DDM, no dopant; (D) 128 μM MPC-C_8 + 32 μM DDM, no dopant. The images were obtained via negative staining of the samples by 2.0% tungstophosphoric acid at pH 6.5. All of the four types of co-assemblies were found to degrade in different degrees before TEM imaging because of desolvation involved in the sample preparation process, despite of their stable and narrowly-dispersed particles sizes in original solutions revealed by DLS. The degradation degree shown in C is relatively low because of the high moisturizing capacity of saccharides.

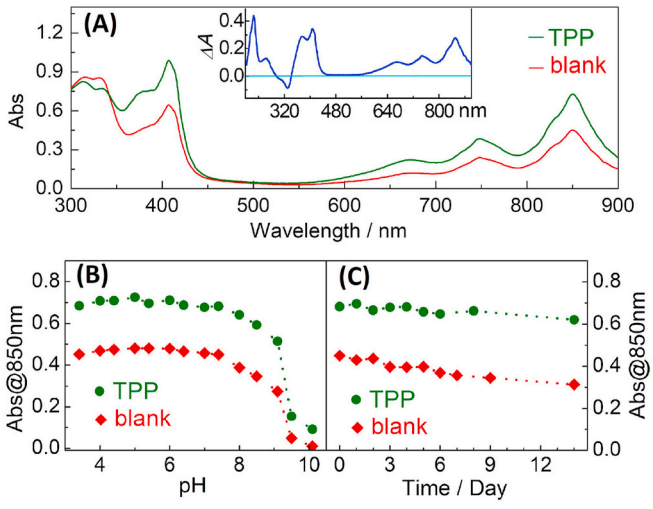

Fig. 4. Comparisons of the absorption behaviour (A), pH dependence (B) and solution stability (C) of the NIR absorbing vesicles before and after TPP doping. Inset of A: the absorbance increase induced by TTP doping. The initial concentrations of TPT-TTF, $TCNQF_4$, MPC-C_8 and TPP were kept at 40 μM, 30 μM, 160 μM and 14 μM, respectively. Solutions for A and C were buffered at pH 7.4 by 10 mM 3,3-dimethylglutaric acid-NaOH. Buffer solutions for B: pH 3.4–7.4: buffered by 10 mM 3,3-dimethylglutaric acid-NaOH; pH 7.4–9.0: buffered by 20 mM Tris-HCl; pH 9.0–10.5: buffered by 20 mM Na_2CO_3–Na_2HCO_3. The solutions in C were kept at 4 °C before test.

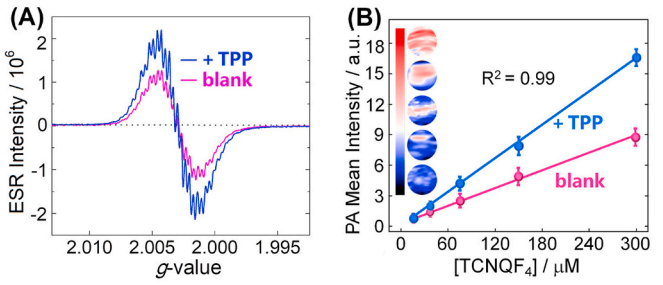

Fig. 5. Comparisons of the ESR (A) and PA (B) performances of the NIR absorbing vesicles before and after TPP doping in aqueous solution at pH 7.4. The molar ratio of TPT-TTF, $TCNQF_4$ and MPC-C_8 was kept at 4 : 3 : 16. The initial concentration of TPT-TTF in A is 40 μM and the doping molar ratio was kept at 35% (vs TPT-TTF).

splitting (Fig. 1B) [43,44]. The NIR absorption of $TCNQF_4^{\bullet-}$ was much stronger than that of the control solution without amphiphiles (Supplementary Fig. S1). However, involvement of the $TCNQF_4^{2-}$ dianions (λ_{max} = 330 nm) in this system was inevitable, and the D-A ratio was then optimized at 4 : 3 to obtain a relatively high yield of $TCNQF_4^{\bullet-}$ (Supplementary Fig. S2). The impact of alkyl chain length of MPC-C_m was investigated and MPC-C_8 was chosen to obtain stable co-assemblies with strong NIR absorption and narrowly-dispersed sizes (Fig. 2).

Common surfactants, such as sodium dodecyl sulfate (SDS) and dodecyl β-D-maltopyranoside (DDM), can be used instead of MPC-C_m to stabilize the chromogenic D-A dyads. TEM imaging revealed that co-assembly of the TPT-TTF-$TCNQF_4$ D-A complex with different surfactants in aqueous solution resulted in the formation of vesicles with particle sizes ranging from 80 nm to 140 nm (Fig. 3). The coordination of π-stacking induced aggregation of the D-A cores with hydrophobic interaction between the lipid chains was concluded to contribute to the low critical vesicle concentrations at 10^{-6} M – 10^{-5} M (TPT-TTF) level.

3.2. Doping of the NIR absorbing vesicles

Doping of the chromogenic D-A ensemble was carried out to improve the spectral performances of the vesicles. Inspired by the molecular doping mechanism of organic transistors [45], the NIR absorption of the vesicles could be modulated by straightforward involvement of hydrophobic n-type dopants, such as triphenylphosphine (TPP) and tri(1-naphthyl)phosphine (TNP), in the radical-generating interlayers. As shown in Fig. 4A, TPP doping significantly enhances NIR absorption of the typical co-assemblies of TPT-TTF, $TCNQF_4$ and MPC-C_8. The conditional absorption coefficient for $TCNQF_4$ at 850 nm increases from 1.50×10^4 M^{-1} cm^{-1} to 2.28×10^4 M^{-1} cm^{-1}, while the average diameter of the vesicles increases from 96 nm to 127 nm at an optimal doping ratio of 35% at pH 7.4 (Supplementary Fig. S3). A reduction of the absorption of $TCNQF_4^{2-}$ at 330 nm was observed to accompany the enhancement of the $TCNQF_4^{\bullet-}$-dominated absorption upon TPP doping. The significant doping effect was attributed to the steric effect and electron donating ability of TPP in modulating the electron transfer between TPT-TTF and $TCNQF_4$. Because of the strong steric effect of TPP, excessive doping with TPP led to degradation of the vesicles and final disappearance of the NIR absorption (Supplementary Fig. S4). Similar phenomenon has been observed upon doping with lower concentration of TNP.

Stability of the vesicles before and after TPP doping in aqueous solution was further examined. The NIR absorption of the vesicles was found almost constant in acidic and near-neutral solutions, while gradually decreasing with increasing pH in basic solutions (Fig. 4B). This was mainly attributed to the saponification of MPC-C_8 and the resulting degradation of the NIR absorbing vesicles. Consistent with this assumption, no obvious difference was observed between the pH depending profiles before and after TPP doping, presumably because

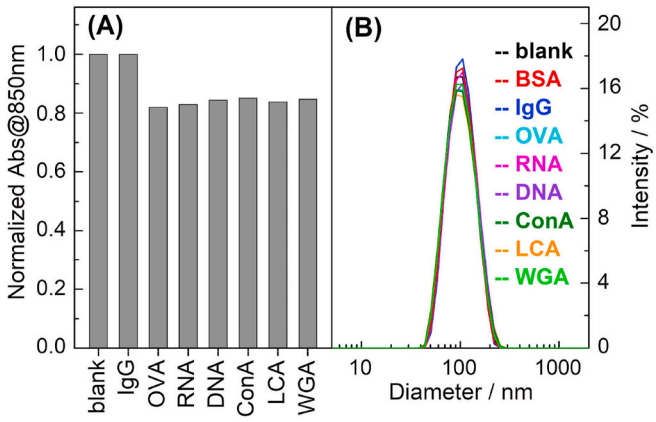

Fig. 6. Changes of absorption (A) and particle sizes (B) of the co-assemblies of TPT-TTF (40 μM), $TCNQF_4$ and MPC-C_8 at a molar ratio of 4 : 3 : 16 in aqueous solution at pH 7.4 upon addition of different biological substances (100 mg/L) including bovine serum albumin (BSA), immunoglobulin (IgG), ovalbumin (OVA), RNA from yeast, DNA from fish sperm, concanvalin A (ConA), lens culinaris agglutinin (LCA) and wheat germ agglutinin (WGA). The mass concentration of the stimuli was equal to that of TPT-TTF. Incubation conditions: 37 °C; 60 min.

that the dopant molecules were embedded in the D-A interlayer. By contrast, the stability of acidic or near-neutral solutions of the vesicles was enhanced after TPP doping. DLS study revealed that the sizes of the vesicles in a near-neutral solution remained almost unchanged within one month. However, the NIR absorption was observed to decrease by ca. 20% in one week even though the solution was stored at 4 °C. This was effectively improved after TPP doping when the decrease in one week was lower than 5% at a TPP doping ratio of 35% (Fig. 4C). These results indicate that a moderate doping creates a new chemical microenvironment good for both the generation and stabilization of $TCNQF_4^{\bullet-}$.

Consistent with absorption spectral evolution, the ESR and photoacoustic (PA) signals of the fabricated vesicles were also improved upon TPP doping. The doped system displays the same ESR spectral profile as that of the undoped one yet with significantly enhanced intensity because of higher concentration of $TCNQF_4^{\bullet-}$ (Fig. 5A). Both of the doped and undoped systems displayed well-resolved hyperfine splitting in their EPR spectra, indicating that the D-A aggregate interlayers of the assembled vesicles are highly ordered that the $TCNQF_4^{\bullet-}$ radicals exist in low spin-exchange regimes. Fluorescence emissions from a series of aromatic fluorophores has been found to be quenched completely when they were employed as the dopants, high PA effect of the fabricated vesicles being therefore expected. Study on the PA performance was carried out *in vitro* and it revealed that TPP doping resulted in a significant enhancement of the PA response upon excitation at 850 nm (Fig. 5B). In both of the doped and undoped systems, NIR PA intensity of the vesicles increased linearly with the concentration of $TCNQF_4$ in aqueous solution at physiological pH. The 35% TPP doped system displayed PA response adequate for imaging at a $TCNQF_4$ concentration of ca. 160 μM, suggesting the potential for bio-imaging application of these NIR absorbing vesicles.

3.3. Functionalization of the NIR absorbing vesicles towards bioanalytical application

Before modification of the fabricated vesicles for anchoring biological targets, the interactions between the unmodified vesicles and biological macromolecules including DNA, RNA and different types of proteins were tested at pH 7.4 and 37 °C. The particle sizes were found to remain almost constant, despite a slight reduction of the NIR absorption after incubation because of the accelerated decay of radicals under biological disturbances (Fig. 6). This indicates that the nonspecific

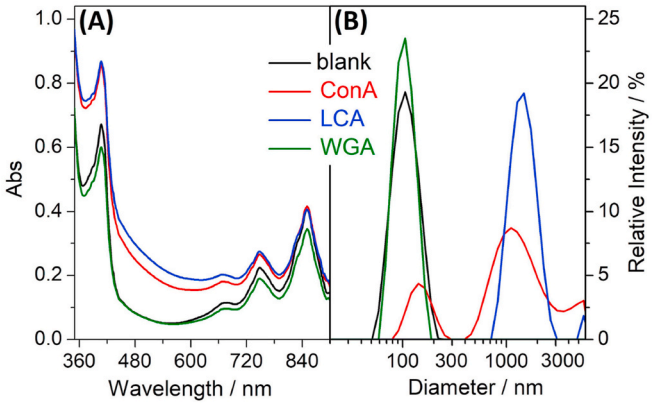

Fig. 7. Absorption spectra (A) and size distributions (B) of the co-assemblies of TPT-TTF (40 μM), $TCNQF_4$ (30 μM), MPC-C_8 (128 μM) and DDM (32 μM) in aqueous solution at pH 7.4 after incubation with different lectins (16 mg/L) at 37 °C for 60 min. The mass concentration of the stimuli was equal to that of DDM.

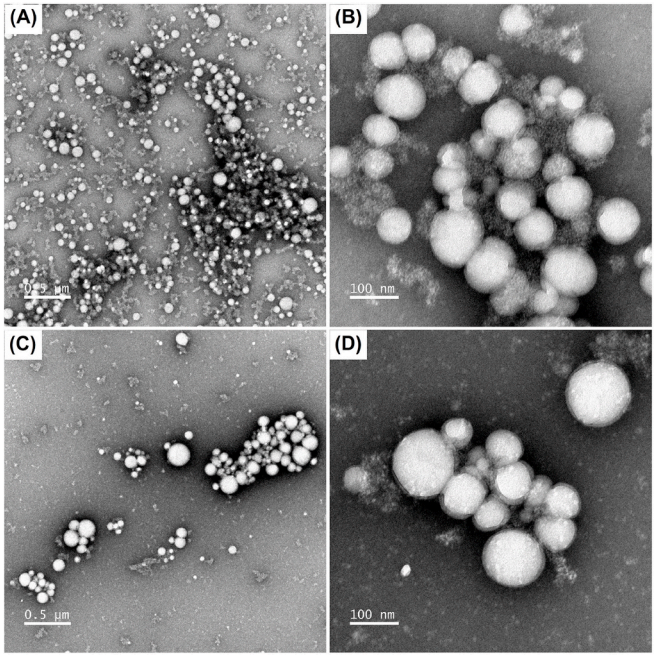

Fig. 8. TEM images of the LCA- (A&B) or ConA-stimulated vesicles (C&D) described in Fig. 7. The samples were negatively stained by 2.0% tungstophosphoric acid at pH 6.5.

adsorption of the fabricated vesicles with biomimetic membrane surfaces is very low.

Compared with the unmodified vesicles, vesicles assembled from mixed amphiphiles of MPC-C_8 and DDM displayed high affinity towards lectins. Serious scattering disturbance appeared in absorption spectra of the ConA- or LCA-titrated solutions while WGA did not induce scattering disturbance (Fig. 7A). This was attributed to the occurrence of cross-linking of the maltopyranoside-modified vesicles by LCA or ConA, since DLS analysis revealed the formation of large particles upon stimulation with LCA or ConA (Fig. 7B). Consistently, the spectral insensitivity towards WGA can be explained by the carbohydrate specificity of lectins that WGA is specific to N-acetyl glycosylamine and therefore of low affinity towards maltopyranoside-modified vesicles [46]. The proposed interaction between the modified vesicles and lectins was confirmed by TEM imaging where the LCA-stimulated (Fig. 8A/B) or ConA-stimulated vesicles (Fig. 8C/D) were crosslinked into large aggregates. These results thus exemplify the successful functionalization of the NIR optical vesicles towards bioanalytical applications via surface modification. Importantly, this pattern of surface modifications can be easily realized by incubation of the vesicles with amphiphiles bearing a bioactive head group in water.

4. Conclusions

In this work, an efficient approach for fabrication of novel NIR absorbing materials has been developed via stabilizing chromogenic radicals in interlayers of lipid membranes. NIR optical vesicles were facilely formed by co-assembly of $TCNQF_4^{\bullet-}$-dominated hydrophobic supramolecular chromophores with surfactants in aqueous solutions. The as-formed dye-interbedded vesicles with biomimetic membrane surfaces displays strong NIR absorption and ESR signals, sensitive PA response upon NIR excitation, and minimal nonspecific interaction with biological macromolecules. Doping of the chromogenic interlayers to optimize the optical properties and modification of the membrane surfaces for anchoring biological targets can be carried out under ambient conditions. This study represents a strategy for developing biological applications of functional ensembles with unique properties yet low stability or solubility in aqueous solution.

Author contributions

S.L. conceived this project. Y.C. (synthesis, characterization, self-assembly, spectral study), J.Z.(bioanalytical application), W.H. (PA tests) and Y.H. (TEM tests) performed the experiments. S.L., Y.C. and Y. J. analysed the experimental data. S.L. and Y.C. wrote the paper, with support from Y.J. All authors discussed the results and contributed to the preparation of the manuscript.

Declaration of competing interest

There are no conflicts to declare.

Acknowledgments

This work was supported by the National Natural Science Foundation of China (NNSFC) (21775129 and 21475111) and the Foundation for Innovative Research Groups of NNSFC (21521004). The authors are grateful for the assistance given by Dr Liming Nie in acquiring PA measurements.

Appendix A. Supplementary data

Supplementary data to this article can be found online at https://doi.org/10.1016/j.dyepig.2020.109076.

References

[1] He S-Q, Song J, Qu J-L, Cheng Z. Crucial breakthrough of second near-infrared biological window fluorophores: design and synthesis toward multimodal imaging and theranostics. Chem Soc Rev 2018;47:4258–78.
[2] Wu D, Chen L-Y, Lee W, Ko G, Yin J, Yoon J. Recent progress in the development of organic dye based near-infrared fluorescence probes for metal ions. Coord Chem Rev 2018;354:74–97.
[3] Guo Z-Q, Park S, Juyoung Yoon J, Shin I. Recent progress in the development of near-infrared fluorescent probes for bioimaging applications. Chem Soc Rev 2014;43:16–29.
[4] Wainwright W. Therapeutic applications of near-infrared dyes. Color Technol 2010;126:115–26.
[5] Hilderbrand SA, Ralph Weissleder R. Near-infrared fluorescence: application to in vivo molecular imaging. Curr Opin Chem Biol 2010;14:71–9.
[6] Zhu S-J, Tian R, Antaris AL, Chen XY, Dai H-J. Near-infrared-II molecular dyes for cancer imaging and surgery. Adv Mater 2019;31:1900321.
[7] Chen Y-S, Li L, Chen W-J, Chen H-Y, Yin J. Near-infrared small molecular fluorescent dyes for photothermal therapy. Chin Chem Lett 2019;30:1353–60.

[8] Yuan L, Lin W-Y, Zheng K-B, He L-W, Huang W-M. Far-red to near infrared analyte-responsive fluorescent probes based on organic fluorophore platforms for fluorescence imaging. Chem Soc Rev 2013;42:622–61.
[9] Luo S-L, Zhang E-L, Su YQ, Cheng TM, Shi CM. A review of NIR dyes in cancer targeting and imaging. Biomaterials 2011;32:7127–38.
[10] Escobedo JO, Rusin O, Lim S, Strongin RM. NIR dyes for bioimaging applications. Curr Opin Chem Biol 2010;14:64–70.
[11] Kiyose K, Kojima H, Nagano T. Functional near-infrared fluorescent probes. Chem Asian J 2008;3:506–15.
[12] Fabian J, Nakazumi H, Matsuoka M. Near-infrared absorbing dyes. Chem Rev 1992;92:1197–226.
[13] Fan Y, Zhang F. A new generation of NIR-II probes: lanthanide-based nanocrystals for bioimaging and biosensing. Adv Optical Mater 2019;7:1801417.
[14] Chang Z, Liu F, Wang L, Deng M-Y, Zhou C-H, Sun Q-C, Chu J. Near-infrared dyes, nanomaterials and proteins. Chin Chem Lett 2019;30:1856–82.
[15] Zhang J-C, Qiao Z-Y, Yang P-P, Pan J, Wang L, Wang H. Recent advances in near-infrared absorption nanomaterials as photoacoustic contrast agents for biomedical imaging. Chin J Chem 2015;33:35–52.
[16] Singh SK. Red and near infrared persistent luminescence nano-probes for bioimaging and targeting applications. RSC Adv 2014;4:58674–98.
[17] Chen L, Han H-Y. Recent advances in the use of near-infrared quantum dots as optical probes for bioanalytical, imaging and solar cell application. Microchim Acta 2014;181:1485–95.
[18] He X-X, Gao J-H, Gambhir SS, Cheng Z. Near-infrared fluorescent nanoprobes for cancer molecular imaging: status and challenges. Trends Mol Med 2010;16:574–83.
[19] Luo X, Li J, Zhao J, Gu L-Y, Qian X-H, Yang Y-J. A general approach to the design of high-performance near-infrared (NIR) D-π-A type fluorescent dyes. Chin Chem Lett 2019;30:839–46.
[20] Patil Y, Misra R. Rational molecular design towards NIR absorption: efficient diketopyrrolopyrrole derivatives for organic solar cells and photothermal therapy. J Mater Chem C 2019;7:13020–31.
[21] Barbieri A, Bandini E, Monti F, Praveen VK, Armaroli N. The rise of near-infrared emitters: organic dyes, porphyrinoids, and transition metal complexes. Top Curr Chem 2016;374:47.
[22] Bricks JL, Kachkovskii AD, Slominskii YL, Gerasov AO, Popov SV. Molecular design of near infrared polymethine dyes: a review. Dyes Pigments 2015;121:238–55.
[23] Hu L, Yan Z-Q, Xu H-Y. Advances in synthesis and application of near-infrared absorbing squaraine dyes. RSC Adv 2013;3:7667–76.
[24] Sun Z, Ye Q, Chi C-Y, Wu J-S. Low band gap polycyclic hydrocarbons: from closed-shell near infrared dyes and semiconductors to open-shell radicals. Chem Soc Rev 2012;41:7857–89.
[25] Tang B-H, Li W-L, Chang Y-C, Yuan B, Wu Y-K, Zhang M-T, Xu J-F, Li J, Zhang X. A supramolecular radical dimer: high-efficiency NIR-II photothermal conversion and therapy. Angew Chem Int Ed 2019;58:15526–31.
[26] Gosztola D, Niemczyk MK, Svec W. Excited doublet states of electrochemically generated aromatic imide and diimide radical anions. J Phys Chem 2000;104:6545–51.
[27] You M-H, Di Y-M, Li M-H, Li H-H, Lin M-J. Persistent radical anions in panchromatic D-A hybrid heterostructures induced by anion-π interactions. Dyes Pigments 2020;180:108468.
[28] Jiao T-Y, Cai K, Nelson JN, Jiao Y, Qiu Y-Y, Wu G-C, Zhou J-W, Cheng C-Y, Shen D-K, Feng Y-N, Liu Z-C, Wasielewski MR, Stoddart F, Li H. Stabilizing the naphthalenediimide radical within a tetracationic cyclophane. J Am Chem Soc 2019;141:16915–22.
[29] Lü B-Z, Chen Y-F, Li P-Y, Wang B, Müllen K, Yin M-Z M. Stable radical anions generated from a porous perylenediimide metal-organic framework for boosting near-infrared photothermal conversion. Nat Commun 2019;10:767.
[30] Cui L-Y, Jiao Y, Wang A-H, Zhao L-Y, Dong Q-Q, Yan X-H, Bai S. Regulating morphologies and near-infrared photothermal conversion of perylene bisimide via sequence-dependent peptide self-assembly. Chem Commun 2018;54:2208–11.
[31] Kang R, Miao R, Qi Y-Y, Chang X-M, Shang C-D, Wang L, Fang Y. Tuning the formation of reductive species of perylene-bisimide derivatives in DMF via aggregation matter. Chem Commun 2017;53:10018–21.
[32] Yang Y-C, He P, Wang Y-X, Bai H-T, Wang S, Xu J-F, Zhang X. Supramolecular radical anions triggered by bacteria in situ for selective photothermal therapy. Angew Chem Int Ed 2017;56:16239–42.
[33] Jiao Y, Liu K, Wang G-T, Wang Y-P, Zhang X. Supramolecular free radicals: near-infrared organic materials with enhanced photothermal conversion. Chem Sci 2015;6:3975–80.
[34] Schmidt D, Bialas D, Wrthner F. Ambient stable zwitterionic, perylene bisimide-centered radical. Angew Chem Int Ed 2015;54:3611–4.
[35] Zhang X, Choi H-A, Lee S, Yin J, Kim SH, Lee C, Yoon J. A cholesteryl thiazolothiazole derivative for colorimetric sensing of Cu2+ and its sol-gel transition. Dyes Pigments 2015;122:109–15.
[36] Liu H-L, Yin G-W, Li Q-Z, Liu G, Pu S-Z, Zhang H-Q. Visible-light-triggered generation of persistent radical anions from perylenediimides: a substituent effect and potential application in photocatalytic reduction of Ag+. Dyes Pigments 2019;165:319–26.
[37] Melby LR, Harder RJ, Hertler WR, Mahler W, Benson RE, Mochel WE. Substituted quinodimethans. II. Anion-radical derivatives and complexes of 7,7,8,8-tetracyanoquinodimethan. J Am Chem Soc 1962;84:3374–87.
[38] Le TH, Lu J-Z, Bond AM, Martin LL. Identification of $TCNQF_4$ redox levels using spectroscopic and electrochemical fingerprints ($TCNQF_4$ = 2,3,5,6-tetrafluoro-7,7,8,8- tetracyanoquinodimethane). Inorg Chim Acta 2013;395:252–4.
[39] Le TH, Nafady A, Qu X-H, Martin LL, Bond AM. Detailed electrochemical analysis of the redox chemistry of tetrafluorotetracyanoquinodimethane $TCNQF_4$, the radical anion $[TCNQF_4]^{\bullet -}$, and the dianion $[TCNQF_4]^{2-}$ in the presence of trifluoroacetic acid. Anal Chem 2011;83:6731–7.
[40] Ferraris J, Cowan DO, Walatka Jr V, Perlstein JH. Electron transfer in a new highly conducting donor-acceptor complex. J Am Chem Soc 1973;95:948–9.
[41] Jain A, Rao KV, Mogera U, Sagade AA, George SJ. Dynamic self-assembly of charge-transfer nanofibers of tetrathiafulvalene derivatives with F_4TCNQ. Chem Eur J 2011;17:12355–61.
[42] Panja S, Kadhane U, Andersen JU, Holm AIS, Hvelplund P, Kirketerp MS, Nielsen SB, Støchkel K. Dianions of 7,7,8,8-tetracyano-p-quinodimethane and perfluorinated tetracyanoquinodimethane: information on excited states from lifetime measurements in an electrostatic storage ring and optical absorption spectroscopy. J Chem Phys 2007;127:124301.
[43] Maity AN, Sarkar B, Niemeyer M, Sieger M, Duboc C, Zalis S, Kaim W. A tetranuclear organorhenium(I) complex of the 2,3,5,6-tetrafluoro7,7,8,8-tetracyano-p-quinodimethane radical anion, $TCNQF_4^{\bullet -}$. Dalton Trans 2008:5749–53.
[44] Maruo T, Rataiczak RD, Jones MT. An ESR study of ion pairing in solutions of the alkali metal salts of tetracyanoquinodimethan (TCNQ) and tetrafluorotetracyanoquinodimethan ($TCNQF_4$). Mol Phys 1991;73:1365–70.
[45] Lüssem B, Keum C, Kasemann D, Naab B, Bao Z, Leo K. Doped organic transistors. Chem Rev 2016;116:13714–51.
[46] Sharon N. Lectins: carbohydrate-specific reagents and biological recognition molecules. J Biol Chem 2007;282:2753–64.